Genesis and bifurcations of unstable periodic orbits in a jet flow

Genesis and bifurcations of unstable periodic orbits in a jet flow

M Yu Uleysky, M V Budyansky and S V Prants

Pacific Oceanological Institute of the Russian Academy of Sciences, 43 Baltiiskaya ulitsa, 690041 Vladivostok, Russia

E-mail: prants@poi.dvo.ru

Abstract
We study the origin and bifurcations of typical classes of unstable periodic orbits in a jet flow that was introduced before as a kinematic model of chaotic advection, transport and mixing of passive scalars in meandering oceanic and atmospheric currents. A method to detect and locate the unstable periodic orbits and classify them by the origin and bifurcations is developed. We consider in detail period-1 and period-4 orbits playing an important role in chaotic advection. We introduce five classes of period-4 orbits: western and eastern ballistic ones, whose origin is associated with ballistic resonances of the fourth-order, rotational ones, associated with rotational resonances of the second and fourth orders and rotational–ballistic ones associated with a rotational–ballistic resonance. It is a new kind of unstable periodic orbits that may appear in a chaotic flow with jets and/or circulation cells. Varying the perturbation amplitude, we track out the origin and bifurcations of the orbits for each class.

PACS numbers: 05.45.Pq, 47.52.+j

1. Introduction

It is well known that a dynamical system is chaotic if it displays sensitivity to initial conditions, has a dense orbit and a dense set of periodic orbits (see, for example, [1]). Periodic orbits play an important role in organizing dynamical chaos in both Hamiltonian and dissipative systems. Stable periodic orbits (SPO) organize a regular motion inside islands of stability in the phase space. Unstable periodic orbits (UPO) form a skeleton around which chaotic dynamics is organized. The motion nearby an UPO is governed by its stable and unstable manifolds. Owing to the density property, the UPOs influence even the asymptotic dynamics. Order and disorder in a chaotic regime are produced eventually by an interplay between sensitivity to initial conditions and regularity of the periodic motion.
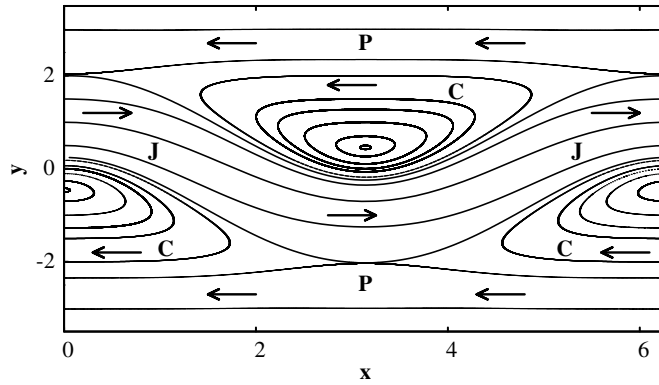
Figure 1. The phase portrait of the model flow (3) in the comoving frame of reference. The first frame with streamlines in the circulation (C), jet (J) and peripheral currents (P) zones is shown. The parameters are: $A = 0.785$, $C = 0.1168$ and $L = 0.628$.

The equations of motion of passive particles advected by any incompressible planar flow are known to have a Hamiltonian form

$$\frac{dx}{dt} = u(x, y, t) = -\frac{\partial \Psi}{\partial y}, \qquad \frac{dy}{dt} = v(x, y, t) = \frac{\partial \Psi}{\partial x}, \tag{1}$$

where the streamfunction Ψ plays the role of a Hamiltonian, and the particle's coordinates x and y are canonically conjugated variables. The phase space of equations (1) is a physical space for advected particles. If the velocity field, $u = u(x, y)$ and $v = v(x, y)$, is stationary, then fluid particles move along streamlines, and the motion is completely regular with any Eulerian stationary field whatever its complexity. A time-periodic velocity field, $u(x, y, t) = u(x, y, t + T)$ and $v(x, y, t) = v(x, y, t + T)$, can produce chaotic particle's trajectories, the phenomenon known as 'chaotic advection' [2, 3].

Study of large-scale advection of water and air masses is one of the key themes in physics of the ocean and atmosphere. Inspite of the complexity of geophysical flows, large-scale coherent structures (jet currents and eddies) are persistent and can clearly be identified on satellite images. Dynamical system techniques have recently been developed to study fluid exchange between a given coherent structure and its surroundings (for recent reviews see [4, 5]) motivated by the problem of transport and mixing of heat, biological tracers, pollutants, etc. It has been shown in a number of papers (see, for example, [4–16]) that chaotic advection [2, 3] is able to produce spatially complex tracer patterns which lead to effective mixing and anomalous transport.

In the present paper we study origin and bifurcations of typical classes of the UPOs in a two-dimensional incompressible flow that has been introduced and analyzed in [4, 6–9] as a toy kinematic model of transport and mixing of passive particles in meandering jet currents in the ocean, like the Gulf Stream, Kuroshio and other main oceanic currents, and in the atmospheric currents like zonal jets with propagating Rossby waves [11, 13, 17].

Among the variety of models of shear flows, one of the simplest ones is a Bickley jet with the velocity profile $\sim \text{sech}^2 y$ and a running wave imposed. It has been introduced in [6, 18] as a simple kinematic model to explain water exchange between the meandering Gulf Stream and its ambient water. The phase portrait of such a flow in the frame, moving with the phase velocity of the running wave, is shown in figure 1. The flow consists of three distinct regions, the eastward jet (J), the circulations (C) and the westward peripheral currents (P)

to the north and south from the jet, separated from each other by the northern and southern ∞-like separatrices. A simple periodic modulation of the wave's amplitude breaks up these separatrices, produces stochastic layers in place of them, and chaotic mixing and transport of passive particles may occur.

In the recent papers [8, 9], we have studied statistical properties of chaotic mixing and transport in such a time-periodic meandering Bickley-jet current and explained some of them by the presence of dynamical traps in the phase space, singular zones in the stochastic layers where particles may spend an arbitrary long but finite time [19]. We identified rotational-islands traps around the boundaries of rotational islands, ballistic-islands traps, around the boundaries of ballistic islands and saddle traps associated with stable manifolds of periodic saddle trajectories [9].

A further insight into chaotic advection in the chosen model flow and in other jet flows is required in order to find a connection between dynamical and topological properties of particle's trajectories forming a complex picture of chaotic mixing. The aim of this paper is to study in detail origin, properties and bifurcations of typical UPOs in the flow considered in [8, 9]. In section 2, we introduce the model streamfunction and advection equations and present a numerical method for locating the UPOs of different periods in chaotic dynamical systems. The method is based on computing a distance d between the positions, $x(t_0)$, $y(t_0)$, of a chosen particle at the moments of time t_0 and $t_0 + mT_0$ (where T_0 is a period of the perturbation and $m = 1, 2, \ldots$), finding local minima of the distance function with given values of m and analyzing them to locate the period-m UPOs for which $d(x(t_0), y(t_0)) = 0$. In section 3, we analyze a saddle orbit (SO) by linearizing the advection equations and study its metamorphoses varying the perturbation amplitude ε. In section 4 we apply the method to study the origin, properties and bifurcations of the period-4 UPOs. We chose namely that period because for sufficiently large values of ε there are no visible period-4 resonances in the phase space. It is easy to locate the UPOs and SPOs of visible resonances on Poincaré sections, but it is not a trivial job to do that with broken resonances. All the period-4 UPOs are classified into five distinct groups which differ by the type of motion of the corresponding particles and their origin and bifurcations. Varying the perturbation amplitude ε, we search for those resonances in each class which generate the corresponding period-4 UPOs and compute bifurcation diagrams for them.

2. Return maps for the model flow

Following to [8, 9], we consider the following streamfunction in the laboratory frame of reference:

$$\Psi'(x', y', t') = -\Psi'_0 \tanh \left(\frac{y' - a \cos k(x' - ct')}{\lambda \sqrt{1 + k^2 a^2 \sin^2 k(x' - ct')}} \right), \tag{2}$$

where the hyperbolic tangent produces the Bickley-jet profile, the square root provides a constant width of the jet λ, and a, k and c are amplitude, wave number and phase velocity of the running wave, respectively. The normalized streamfunction in the frame moving with c is

$$\Psi = -\tanh \left(\frac{y - A \cos x}{L \sqrt{1 + A^2 \sin^2 x}} \right) + Cy, \tag{3}$$

where $x = k(x' - ct')$ and $y = ky'$ are new scaled coordinates. The normalized jet's width $L = \lambda k$, wave's amplitude $A = ak$ and phase velocity $C = c/\Psi'_0 k$ are the control parameters. The advection equations (1) with the streamfunction (3) have the following form

in the comoving frame:

$$\dot{x} = \frac{1}{L\sqrt{1 + A^2 \sin^2 x}\cosh^2 \theta} - C, \qquad \dot{y} = -\frac{A \sin x(1 + A^2 - Ay \cos x)}{L(1 + A^2 \sin^2 x)^{3/2}\cosh^2 \theta},$$

$$\dot{\theta} = \frac{y - A \cos x}{L\sqrt{1 + A^2 \sin^2 x}}, \tag{4}$$

where the dot denotes differentiation with respect to the scaled time $t = \Psi'_0 k^2 t'$.

The flow with the streamfunction (2) is steady in the comoving frame and its phase portrait is shown in figure 1. There are southern and northern sets of elliptic fixed points: $x_e^{(s)} = 2\pi n$, $y_e^{(s)} = -L\,\mathrm{Arcosh}\,\sqrt{1/LC} + A$ and $x_e^{(n)} = (2n+1)\pi$, $y_e^{(n)} = L\,\mathrm{Arcosh}\,\sqrt{1/LC} - A$, respectively, and the southern and northern sets of hyperbolic (saddle) fixed points: $x_s^{(s)} = (2n+1)\pi$, $y_s^{(s)} = -L\,\mathrm{Arcosh}\,\sqrt{1/LC} - A$ and $x_s^{(n)} = 2\pi n$, $y_s^{(n)} = L\,\mathrm{Arcosh}\,\sqrt{1/LC} + A$, respectively, where $n = 0, \pm 1, \dots$.

A perturbation is provided by a periodic modulation of the wave's amplitude

$$A(t) = A_0 + \varepsilon \cos(\omega t + \varphi). \tag{5}$$

The equations of motion (4) are symmetric under the following transformations: $t \to t$, $x \to \pi + x$, $y \to -y$ and $t \to -t$, $x \to -x$, $y \to y$. Due to these symmetries, the motion can be considered in the northern chain of the circulation cells on the cylinder with $0 \leqslant x \leqslant 2\pi$. The part of the phase space with $2\pi n \leqslant x \leqslant 2\pi(n+1)$, $n = 0, \pm 1, \dots$, is called *a frame*. The first frame is shown in figure 1. The values of the following control parameters are fixed in our simulation: $L = 0.628$, $A_0 = 0.785$, $C = 0.1168$, $T_0 = 2\pi/\omega = 24.7752$ and $\varphi = \pi/2$. The only varying parameter is the perturbation amplitude ε.

In fluid mechanics an infinite number of initial conditions come in play simultaneously and a number of fluid elements, launched in different places, may follow the same orbit on the flow plane. Essentially, a number of particles with different initial positions may move along the same orbit. More precisely, *an orbit* is a set of points $\{x_i, y_i\}(i = 1, 2, \dots)$ on the phase plane (on the flow plane) with the following two properties: (i) there exists for $\forall i, j$ an integer k (positive or negative) such that

$$\begin{pmatrix} x_i \\ y_i \end{pmatrix} = \hat{U}(kT_0) \begin{pmatrix} x_j \\ y_j \end{pmatrix}, \tag{6}$$

where $\hat{U}$ is an evolution operator; and (ii) there exists for $\forall i, k$ an integer j such that

$$\hat{U}(kT_0) \begin{pmatrix} x_i \\ y_i \end{pmatrix} = \begin{pmatrix} x_j \\ y_j \end{pmatrix}. \tag{7}$$

A period-m orbit is a finite set of points on the phase plane with the properties (6) and (7) consisting of m elements. Thus, any period-m orbit contains m points whose trajectories belong to this orbit.

To locate the UPOs in the phase space we fix values of the control parameters and compute with a large number of particles the Euclidean distance $d = \sqrt{[x(t_0 + mT_0) - x(t_0)]^2 + [y(t_0 + mT_0) - y(t_0)]^2}$ between particle's position at an initial moment of time t_0 and at the moments of time $t_0 + T = t_0 + mT_0$, where $m = 1, 2, \dots$. The data are plotted as *a period-m return map* (RM) that shows by color the values of d for particles with initial positions $[x(t_0), y(t_0)]$. At the first stage, we select a large number of points where the function $d(x(t_0), y(t_0))$ may have local minima. Then we apply the method of a downhill simplex to localize the minima in neighbourhoods of those points [20]. There are such minima among them for which $d = 0$ with a given value of m. The procedure allows us to detect both UPOs and SPOs not only in periodically perturbed Hamiltonian systems but in any chaotic system.
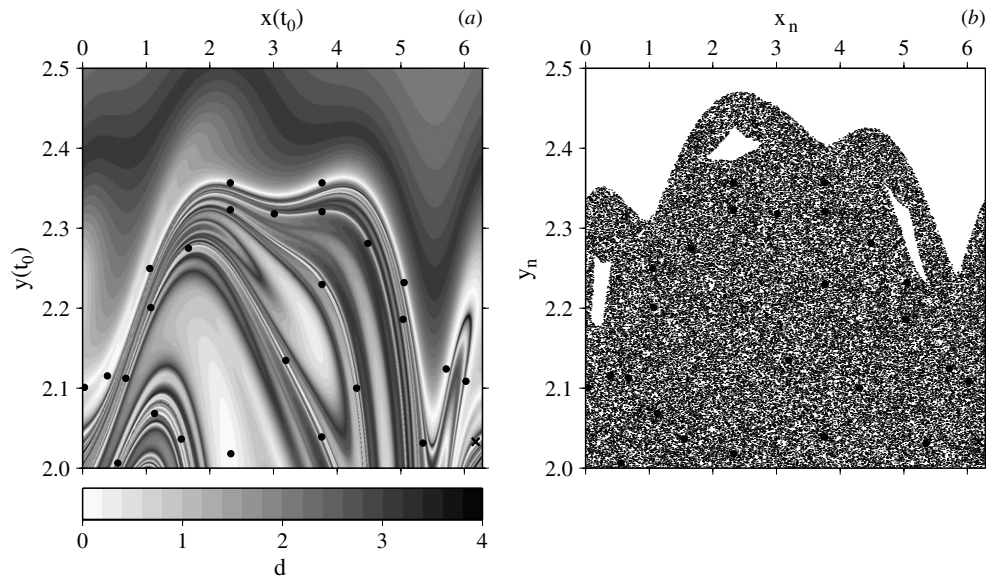
Figure 2. (*a*) Period-4 return map representing the distance d between particle's position $x(t_0)$ and $y(t_0)$ at t_0 and its position at $t_0 + 4T_0$. Cross marks location of the saddle trajectory and dots mark initial positions of trajectories of the period-4 UPOs. (*b*) Poincaré section of the northern separatrix layer with positions of those dots.

Return maps with $m = 1, 2, 3, 4$ and 12 have been computed. In the next section we consider the SO which is a period-1 UPO. The main efforts are devoted to analysis of period-4 UPOs because it is not a trivial task to detect the UPOs when the corresponding resonances cannot be identified on Poincaré sections. It is the case with $m = 4$. The period-4 RM is shown in figure 2(*a*) with the cross marking location of the period-1 saddle trajectory and black dots marking initial positions of 26 trajectories of the period-4 UPOs with a relative accuracy 10^{-13}–10^{-14}. For comparison, we demonstrate in figure 2(*b*) locations of those dots on the Poincaré section. It is evident that they cannot be prescribed to any structures in the phase space and cannot be identified by inspection of the Poincaré section.

3. Saddle orbit

The saddle points of the unperturbed equations of motion (4), $\left(x_s^{(n)}, y_s^{(n)}\right)$ and $\left(x_s^{(s)}, y_s^{(s)}\right)$, become period-1 saddle orbits (SO) under the periodic perturbation (5). To analyze such a SO we linearize the perturbed equations

$$\dot{x} = X(x, y), \qquad \dot{y} = Y(x, y) \tag{8}$$

in a neighborhood of the saddle point

$$x_s = 0, \qquad y_s = L \operatorname{Arcosh} \sqrt{\frac{1}{LC}} + A_0, \tag{9}$$

where $X(x, y)$ and $Y(x, y)$ are the right-hand sides of the corresponding equations in the set (4) with A being the time-periodic amplitude (5). After linearizing, we get the following

5

equations for small deviations $\eta \equiv x - x_s$ and $\xi \equiv y - y_s$:

$$\dot{\eta} = \frac{1}{L\cosh^2\Theta} - C - \frac{2\tanh\Theta}{L^2\cosh^2\Theta}\xi, \qquad \dot{\xi} = \frac{A(AL\Theta - 1)}{L\cosh^2\Theta}\eta, \qquad (10)$$

where

$$\Theta \equiv \operatorname{Arcosh}\sqrt{\frac{1}{LC} - \frac{\varepsilon\cos\Phi}{L}}, \qquad \Phi \equiv \omega t + \varphi.$$

For small values of the perturbation amplitude ε, it is possible to simplify the set (10) expanding the right-hand sides in a series in powers of $\varepsilon\cos\Phi$ and neglecting terms above the first order. In terms of the variables

$$X_s = \lim_{\varepsilon\to 0} X(x_s, y_s), \qquad X_{ys} = \lim_{\varepsilon\to 0} X_y(x_s, y_s), \qquad Y_{xs} = \lim_{\varepsilon\to 0} Y_x(x_s, y_s),$$

$$X_\varepsilon = \lim_{\varepsilon\to 0}\frac{\partial X(x_s, y_s)}{\partial(\varepsilon\cos\Phi)}, \qquad X_{y\varepsilon} = \lim_{\varepsilon\to 0}\frac{\partial X_y(x_s, y_s)}{\partial(\varepsilon\cos\Phi)}, \qquad Y_{x\varepsilon} = \lim_{\varepsilon\to 0}\frac{\partial Y_x(x_s, y_s)}{\partial(\varepsilon\cos\Phi)},$$

$$X_x(x, y) = \frac{\partial X(x, y)}{\partial x}, \qquad X_y(x, y) = \frac{\partial X(x, y)}{\partial y}, \qquad (11)$$

$$Y_x(x, y) = \frac{\partial Y(x, y)}{\partial x}, \qquad Y_y(x, y) = \frac{\partial Y(x, y)}{\partial y}$$

we get the following equations of the first order in $\varepsilon\cos\Phi$:

$$\dot{\eta} = X_s + X_{ys}\xi + \varepsilon\cos\Phi(X_\varepsilon + X_{y\varepsilon}\xi), \qquad \dot{\xi} = (Y_{xs} + \varepsilon\cos\Phi Y_{x\varepsilon})\eta, \qquad (12)$$

where

$$X_s = 0, \qquad X_{ys} = -\frac{2C\sqrt{1 - LC}}{L}, \qquad Y_{xs} = A_0 C(A_0 L\operatorname{Arsech}\sqrt{LC} - 1),$$

$$X_\varepsilon = \frac{2C\sqrt{1 - LC}}{L}, \qquad X_{y\varepsilon} = \frac{2C(3LC - 2)}{L^2}, \qquad (13)$$

$$Y_{x\varepsilon} = \frac{C\big(2A_0 L(L + A_0\sqrt{1 - LC})\operatorname{Arsech}\sqrt{LC} - 2A_0\sqrt{1 - LC} - L(1 + A_0^2)\big)}{L}.$$

Coming back to set (10) and expanding the equations up to the second order in $\varepsilon\cos\Phi$, we obtain the equations

$$\dot{\eta} = X_s + X_{ys}\xi + \varepsilon\cos\Phi(X_\varepsilon + X_{y\varepsilon}\xi) + \frac{\varepsilon^2}{2}\cos^2\Phi(X_{\varepsilon^2} + X_{y\varepsilon^2}\xi),$$

$$\dot{\xi} = \left(Y_{xs} + \varepsilon\cos\Phi Y_{x\varepsilon} + \frac{\varepsilon^2}{2}\cos^2\Phi Y_{x\varepsilon^2}\right)\eta, \qquad (14)$$

with the following notations:

$$Y_{x\varepsilon^2} = \lim_{\varepsilon\to 0}\frac{\partial^2 Y_x(x_s, y_s)}{\partial(\varepsilon\cos\Phi)^2} = -\frac{2C}{L^2}\Big[A_0(2L^2 - 3LC + 2) + 2L(1 + A_0^2)\sqrt{1 - LC}$$

$$- L(L^2 + A_0^2(2 - 3LC) + 4A_0 L\sqrt{1 - LC})\operatorname{Arsech}\sqrt{LC}\Big],$$

$$X_{\varepsilon^2} = \lim_{\varepsilon\to 0}\frac{\partial^2 X(x_s, y_s)}{\partial(\varepsilon\cos\Phi)^2} = \frac{2C(2 - 3LC)}{L^2}, \qquad (15)$$

$$X_{y\varepsilon^2} = \lim_{\varepsilon\to 0}\frac{\partial^2 X_y(x_s, y_s)}{\partial(\varepsilon\cos\Phi)^2} = \frac{8C\sqrt{1 - LC}(3LC - 1)}{L^3}.$$

In the following, we compare numerically some properties of the SOs, generated from the same fixed point (x_s, y_s), with the main equations of motion (8), linearized equations (10), linearized equations (12) with $O(\varepsilon)$ and equations (14) with $O(\varepsilon^2)$. Simulation shows that
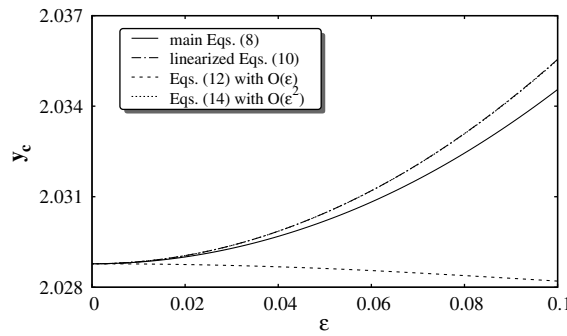
Figure 3. Dependence of the *y*-coordinate of the central point y_c of the SO on the perturbation amplitude ε with different versions of advection equations.
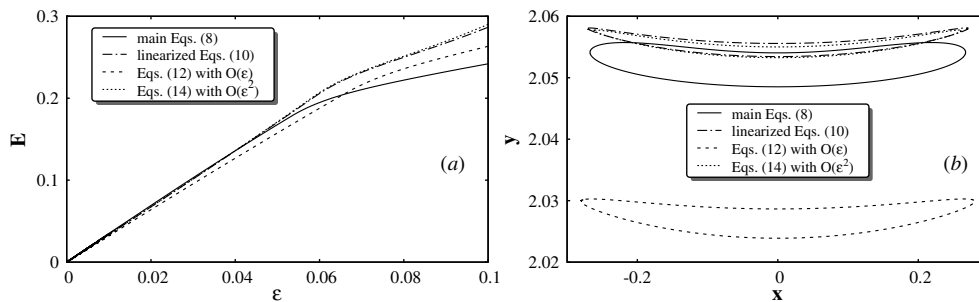

Figure 4. (*a*) Dependence of deviation of the SO form from ellipticity *E* on the perturbation amplitude ε and (*b*) the form of the SO at $\varepsilon = 0.2$.

dependence of *x*-coordinate of the initial position of the SO on the perturbation amplitude ε is practically the same with all the versions of the advection equations listed above. As ε increases, the *x*-coordinate shifts to the west from the point $x_s = 0$. As to *y*-coordinate, it moves to the north with increasing ε in a similar way for equations (8), (10) and (14), but its behavior differs strongly for the first-order equations in ε (12). In figure 3 we demonstrate the ε-dependence of the *y*-coordinate of the central point y_c of the SO which is a central point between maximal and minimal values of *y*. In all the cases, $x_c = 0$ is the *x*-coordinate of the central point. It is evident that equations of the first order in ε cannot give a correct position of the SO. The ε-dependence of deviation of the form of the SO from ellipticity *E* is shown in figure 4(*a*), where *E* is the ratio of the area between the SO and an ellipse with semi-axes equal to the height and width of the SO to the area of the ellipse. Figure 4(*b*) demonstrates that the form of the SO does not change dramatically after linearization, but its position in the phase space cannot be found correctly in the first order in ε. We may conclude that even with small values of the perturbation amplitude the effect of the second harmonic 2ω is not small.

4. Origin and bifurcations of unstable periodic orbits

In this section we analyze the origin of the period-4 UPOs and their bifurcations that occur with changing the perturbation amplitude ε. Using the period-4 RM (figure 2(*a*)), we located
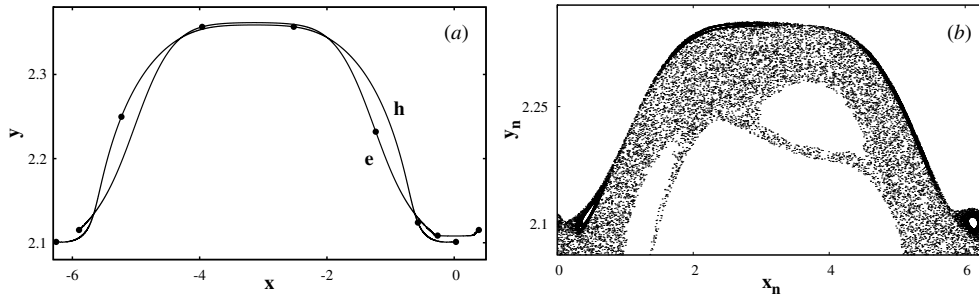
Figure 5. (*a*) Two $C_{WB}^{4:1}$ western ballistic period-4 UPOs at $\varepsilon = 0.0785$ with initial positions of four unstable periodic trajectories belonging to each of them. The *e* and *h* orbits were born from the elliptic and hyperbolic points of the northern ballistic resonance 4:1, respectively. (*b*) The Poincaré section at $\varepsilon = 0.005$ with the northern ballistic resonance 4:1 consisting of four ballistic islands along the northern border of the separatrix layer.

all the period-4 UPOs and the initial positions of four trajectories for each of them. They differ by the type of motion of the passive particles and their length *l* which is a length of the corresponding curve between two positions on the orbit separated by the time interval $4T_0$. On the cylinder $0 \leqslant x \leqslant 2\pi$, all the UPOs are closed curves whose topology may be very complicated. In the physical space, the UPOs can be classified as rotational ones (particles rotate in the same frame), ballistic ones (particles move ballistically from a frame to frame) and rotation–ballistic ones (particles may rotate for a while in a frame, then move ballistically through a few frames and change their direction of motion).

4.1. $C_{WB}^{4:1}$ class: western ballistic UPOs associated with the 4:1 western ballistic resonance

The shortest ones among all the period-4 UPOs are western ballistic UPOs. The particles belonging to the $C_{WB}^{4:1}$ class move in a periodic way to the west along such an orbit in the northern separatrix layer which appears between the northern (C) and (P) regions in figure 1 as a result of the perturbation. With the help of the RM in figure 2(*a*), we located two $C_{WB}^{4:1}$ orbits with initial positions of four periodic trajectories belonging to each of them. In order to track out the origin of the *e* and *h* orbits, shown in figure 5(*a*) at $\varepsilon = 0.0785$, we decrease the value of the perturbation amplitude ε, compute the corresponding period-4 RMs, locate the $C_{WB}^{4:1}$ orbits and measure their length.

The result may be resumed as follows. The western ballistic resonance 4:1 with four elliptic and four hyperbolic points appears under a perturbation with a very small value of ε. On the Poincaré section in figure 5(*b*) at $\varepsilon = 0.005$, it is manifested as four ballistic islands along the northern border of the separatrix layer. Two of the islands are so thin that they are hardly visible in the figure. With increasing ε, the size of the resonance decreases and at the critical value $\varepsilon \approx 0.016$ it vanishes (see figure 2(*b*) where there are no signs of that resonance at $\varepsilon = 0.0785$). The orbit, associated with the elliptic fixed points of the western resonance 4:1, loses its stability and bifurcates into the $C_{WB}^{4:1}$ UPO of period-4 which we denote by the symbol *e*. Its length practically does not change with increasing ε (see figure 6). The length *l* of the *h* orbit, associated with the hyperbolic points of the that resonance, changes dramatically at $\varepsilon \approx 0.0715$ (see figure 6) increasing fast after this point because of appearance of a meander and a loop on the *h* orbit nearby the SO.
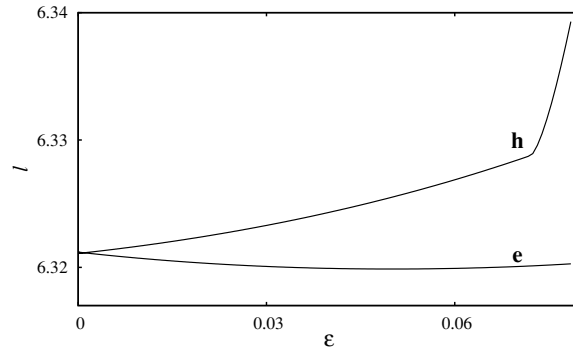
8

Figure 6. Dependence of the length l of the e and h $C_{WB}^{4:1}$ western ballistic UPOs on the perturbation amplitude ε.
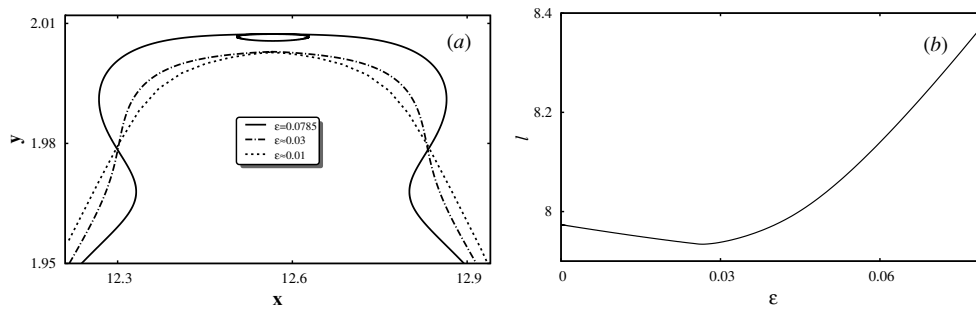

Figure 7. (*a*) Metamorphoses of the h $C_{EB}^{4:1}$ eastern ballistic UPO as the perturbation amplitude ε changes: solid line, $\varepsilon = 0.0785$; dashed line, $\varepsilon = 0.03$; and dotted line, $\varepsilon = 0.01$. (*b*) Dependence of the length l of the h $C_{EB}^{4:1}$ orbit on the perturbation amplitude ε.

4.2. $C_{EB}^{4:1}$ class: eastern ballistic UPOs associated with the 4:1 eastern ballistic resonance

The eastern ballistic UPOs of period-4 lie in the southern separatrix layer between the (J) and (C) regions (see figure 1) to the north from the jet. Particles move along such orbits to the east in a periodic way. The origin and bifurcations of the $C_{EB}^{4:1}$ orbits are similar to the western ballistic ones. They appear from elliptic and hyperbolic points of the eastern ballistic resonance 4:1 as ε increases. The elliptic orbit of this resonance loses it stability and bifurcates into the UPO of the e-type. The hyperbolic orbit changes its topology, transforming from the bell-like curve at $\varepsilon = 0.01$ to the curve with a meander and a loop nearby the SO at $\varepsilon = 0.0785$ (see figure 7(*a*)). The length l of the h orbit in figure 7(*b*) decreases with increasing ε up to the bifurcation point $\varepsilon \approx 0.0275$, after which it increases fast due to the complexification of the orbit's form (see figure 7(*a*)).

4.3. $C_R^{4:1}$ class: orbits associated with the 4:1 rotational resonance

Four different orbits in the $C_R^{4:1}$ class, located with the help of the period-4 RM, are shown in figure 8 at $\varepsilon = 0.0785$ along with initial positions of four unstable periodic trajectories on each of them. The corresponding fluid particles rotate in the same frame along closed curves. The genesis of the $C_R^{4:1}$ orbits is the following. A 4:1 rotational resonance appears under a small
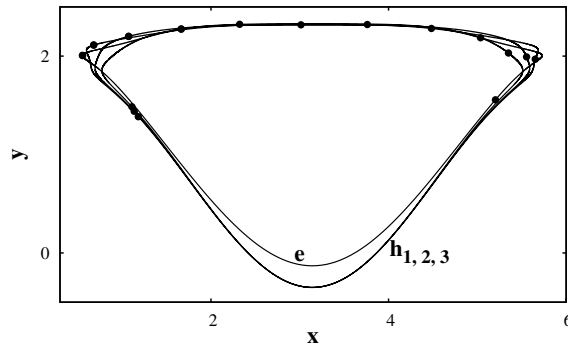
Figure 8. Four 4:1 rotational UPOs of the $C_R^{4:1}$ class with initial positions of four unstable periodic trajectories belonging to each of them. The e and $h_{1,2,3}$ orbits were born from the elliptic and hyperbolic points of the 4:1 rotational resonance, respectively ($\varepsilon = 0.0785$).
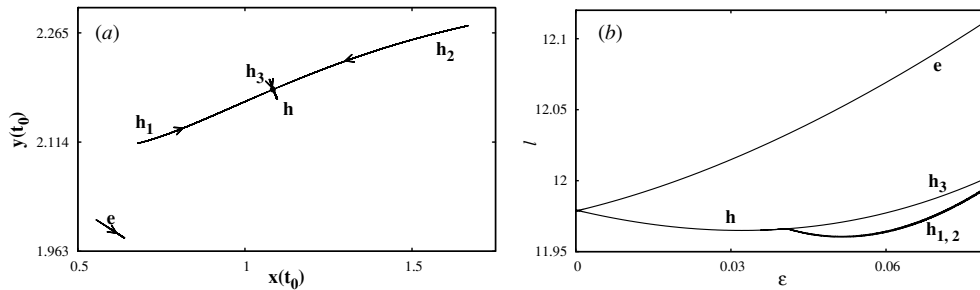

Figure 9. (*a*) Movement of initial positions ($x(t_0)$, $y(t_0)$) of the rotational 4:1 UPOs with decreasing the perturbation amplitude is shown by arrows. The black circle is a pitchfork bifurcation point at $\varepsilon \approx 0.040945$ where the hyperbolic orbit of the resonance h bifurcates into three different orbits h_1, h_2 and h_3. (*b*) Bifurcation diagram $l(\varepsilon)$.

perturbation (5). As the amplitude ε increases, its elliptic orbit loses stability and bifurcates at $\varepsilon \approx 0.003$ into the UPO which we denote by the symbol e. The hyperbolic orbit of the 4:1 resonance h bifurcates at $\varepsilon \approx 0.040945$ into two hyperbolic orbits, h_1, h_2, and an elliptic orbit h_3 in the centers of four stability islands. It is a pitchfork bifurcation. In figure 9(*a*) we show by arrows a movement of initial positions of the $C_R^{4:1}$ orbits as ε decreases. The pitchfork bifurcation point is shown as a black circle. As ε increases further, the elliptic orbit h_3 loses its stability and becomes a hyperbolic $C_R^{4:1}$ orbit.

4.4. $C_R^{2:1}$ class: orbits associated with the 2:1 rotational resonance

The class $C_R^{2:1}$ consists of two rotational UPOs, associated with the 2:1 rotational resonance, with elliptic and hyperbolic orbits and two periodic trajectories on each of them. The resonance appears under a small perturbation. At $\varepsilon \approx 0.0665$, the elliptic orbit of this resonance undergoes a period doubling bifurcation into a period-4 elliptic orbit with four trajectories and a period-2 hyperbolic orbit with two trajectories. The latter is shown in figure 10(*a*) at $\varepsilon = 0.0785$. The Poincaré section of the 2:1 rotational resonance at $\varepsilon = 0.0668$ (just after the bifurcation) is shown in figure 10(*b*). By further increasing ε, we see that the resonance 2:1 vanishes, and the period-4 elliptic orbit loses its stability and bifurcates into a period-4
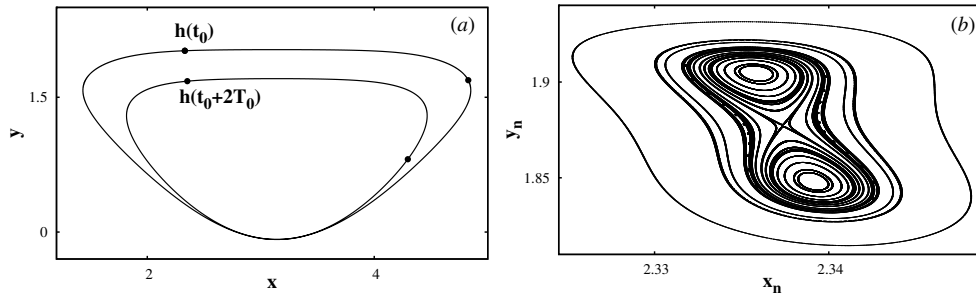
Figure 10. (*a*) 2:1 rotational UPOs with initial positions of 4 unstable periodic trajectories ($\varepsilon = 0.0785$). (*b*) Poincaré section of the 2:1 rotational resonance at $\varepsilon = 0.0668$ (just after the period doubling bifurcation).
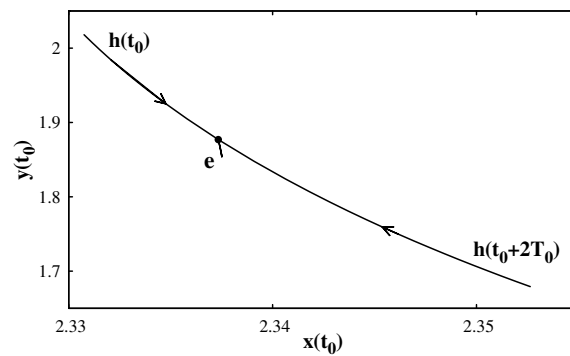

Figure 11. Emergency of the doubly-branched UPO, shown in figure 10(*a*), from the elliptic orbit of the 2:1 rotational resonance at the bifurcation point (black circle). Movement of fixed initial points on the upper $h(t_0)$ and lower $h(t_0 + 2T_0)$ branches to the bifurcation point with decreasing ε is shown.

UPO. To clarify this bifurcation we fix a point at the moment t_0 on the upper branch of the orbit in figure 10(*a*) and another point on the lower branch at $t = t_0 + 2T_0$ and scan their positions when decreasing the perturbation amplitude ε. Figure 11 demonstrates clearly that the points move to the position of the elliptic orbit of the 2:1 resonance and merge with it at the bifurcation point.

4.5. $C_{RB}^{4:1}$ class: rotation–ballistic UPOs associated with the rotational–ballistic resonance

The class $C_{RB}^{4:1}$ consists of four period-4 UPOs shown in figure 12(*a*). We call those orbits as rotational-ballistic (RB) ones because the corresponding particles begin to move to the west in one frame, then turn to the east and travel in the southern separatrix layer to the next frame, fulfil one turnover in this frame and repeat their motion to the east. The genesis of the $C_{RB}^{4:1}$ orbits differs from the genesis of the other classes of period-4 UPOs. Each of the resonances, associated with $C_{WB}^{4:1}$, $C_{EB}^{4:1}$, $C_R^{4:1}$ and $C_R^{2:1}$, appears under an infinitely small perturbation amplitude ε. Rotation–ballistic motion of period-m and corresponding orbits cannot in principle appear in the flow below some critical value of ε (which depends on m) because the width of the stochastic layers (which increases with increasing ε) should be large
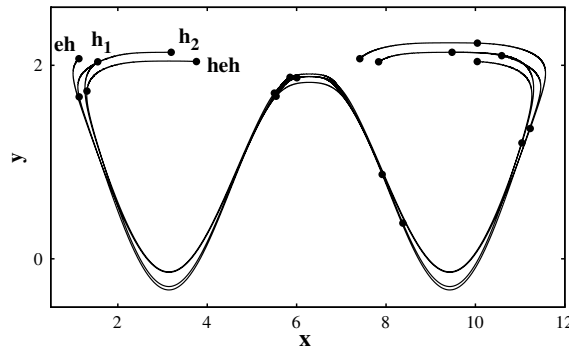
Figure 12. Four rotational–ballistic period-4 UPOs with their initial positions in the phase space eh, h_1, h_2 and heh. The other points are the initial positions of the corresponding trajectories.
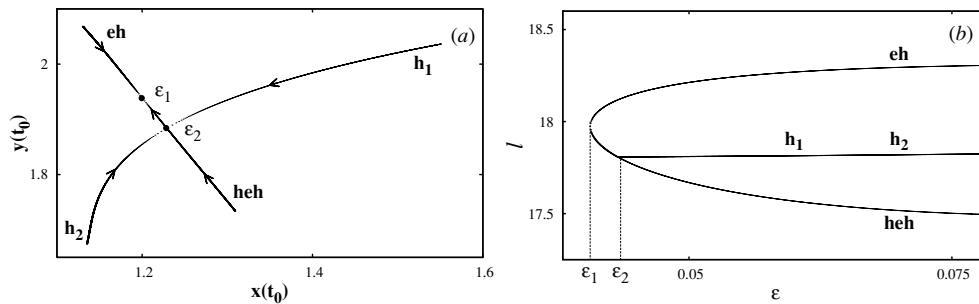

Figure 13. (*a*) At the saddle-center bifurcation point $\varepsilon = \varepsilon_1 \approx 0.040\,715$, there appears a RB 4:1 resonance with the elliptic orbit eh which loses its stability with increasing ε. The hyperbolic orbit of the RB resonance bifurcates at $\varepsilon = \varepsilon_2 \approx 0.0433$ into two hyperbolic period-4 UPOs h_1 and h_2 and the elliptic orbit heh which loses its stability with further increasing ε. (*b*) Bifurcation diagram $l(\varepsilon)$.

enough in order that particles would have enough time to travel the corresponding distance to the east and west.

The genesis and evolution of the $C_{\mathrm{RB}}^{4:1}$ UPOs are shown schematically on the bifurcation diagrams in figure 13. In figure 13(*a*) we demonstrate movement in the phase space of initial positions of the $C_{\mathrm{RB}}^{4:1}$ orbits with decreasing the perturbation amplitude ε. The dependence of the lengths of those orbits on ε is shown in figure 13(*b*).

The rotational–ballistic 4:1 resonance appears at a critical value of the perturbation amplitude $\varepsilon = \varepsilon_1 \approx 0.0407\,15$ as the result of the saddle-center bifurcation and manifests itself as four small islands of stability on the corresponding Poincaré section. One of these islands is shown in figure 14(*a*). If ε increases further, the elliptic orbit eh in the centers of the RB 4:1 resonance loses its stability and becomes a hyperbolic RB period-4 orbit. The hyperbolic orbit h of the RB resonance at $\varepsilon = \varepsilon_2 \approx 0.0433$ undergoes a pitchfork bifurcation into two hyperbolic RB period-4 orbits h_1 and h_2 and the elliptic orbit heh in the centers of the new period-4 RB resonance one of whose stability islands is shown in figure 14(*b*). By further increasing ε, the elliptic orbit heh loses its stability and becomes a hyperbolic RB period-4 orbit.
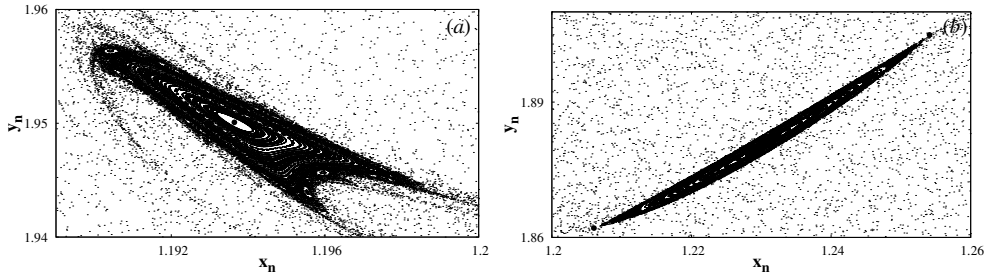
Figure 14. (*a*) One of the stability islands of the RB 4:1 resonance appearing after the saddle-center bifurcation at $\varepsilon = 0.040\,72 \gtrsim \varepsilon_1$ with the elliptic point *eh* in its center. (*b*) One of the stability islands of the RB 4:1 resonance appearing after a pitchfork bifurcation at $\varepsilon = 0.0435 \gtrsim \varepsilon_2$ with the elliptic point *heh* in its center.

5. Conclusion

We have developed a method to track unstable periodic orbits based on computing and analyzing local minima of the distance function $d(x(t_0), y(t_0))$. The method is not restricted to our simple Hamiltonian system with a periodic perturbation and is applicable to a variety of chaotic systems. The results, obtained with our specific model of a meandering jet, can be resumed as follows.

We detected and located the UPOs of periods 1 and 4. Varying the perturbation amplitude, we have found bifurcations of the period-4 orbits, the UPOs of the lowest period with non-trivial origin. Those orbits have been grouped into five classes by their origin and bifurcations. $C_{WB}^{4:1}$ $\left(C_{EB}^{4:1}\right)$ class consists of the western (eastern) ballistic UPOs associated with the 4:1 western (eastern) ballistic resonance. $C_R^{4:1}$ $\left(C_R^{2:1}\right)$ class consists of the rotational UPOs associated with the 4:1 (2:1) rotational resonance. $C_{RB}^{4:1}$ class consists of specific rotational-ballistic UPOs associated with 4:1 rotational-ballistic resonance.

We would like to stress the following. Rotational and ballistic resonant islands are well-known objects in the phase space of Hamiltonian systems [21]. As far as we know, rotation–ballistic resonant islands of stability have not been found before. They are expected to appear as well in other jet-flow models (kinematic and dynamic ones) under specific values of control parameters, and it would be interesting to search for them in the models introduced in [4, 6–9, 11–17, 22, 23]. Like ballistic islands, the rotation–ballistic islands should affect transport and its statistical characteristics. Due to the presence of rotation phase of motion, the mean drift velocity of RB particles is smaller than that for ballistic particles. It is expected that boundaries of the rotational-ballistic islands are specific dynamical traps that should affect transport and statistical properties of passive particles and may be treated by the methods developed in [9]. Properties of rotational–ballistic islands traps may differ from properties of rotational-islands traps and ballistic-islands traps because of different locations of the corresponding hyperbolic points around the islands. In the chains of rotational and ballistical islands, they appear to be between the islands, whereas in the case of RB islands they are situated either on one (a saddle-center bifurcation) or both sides (a pitchfork bifurcation) of a given island.

In addition, by linearizing the advection equations, we have studied the properties of the period-1 saddle orbits playing a crucial role in chaotic transport and mixing of passive particles. Stable and unstable manifolds of UPOs are material curves of complicated forms which cannot be crossed by particle's trajectories. Their role in transport and mixing of passive particles

13

in the meandering jet flow considered is significant because they separate trajectories with different dynamical and topological properties. The UPOs found in this paper act as dynamical traps where particles and their trajectories may spend a rather long time before escaping. It was checked by computing distributions of the escape times for the period-4 UPOs and the saddle orbit. The rotational UPOs should contribute to statistics of comparatively short flights (see figure 5 in [9]). The UPOs with larger values of the period can be classified into three big groups: ballistic, rotational and rotation–ballistic ones. The origin and bifurcations of the orbits in each class can be studied in a similar way, but it may require larger computational efforts.

The results obtained do not depend critically on the exact form of the streamfunction and chosen values of the control parameters. The UPOs in other kinematic and dynamical models of geophysical jets, known in the literature [11–17, 22, 23], can be detected, located and classified in a similar way. The UPOs form the skeleton for chaotic advective mixing and transport in fluid flows, and knowledge of them (at least, lower-period ones) allows us to analyze complex, albeit rather regular, stretching and folding structures in the flows.

Acknowledgments

References

[1] Guckenheimer J and Holmes P 1983 *Nonlinear Oscillations, Dynamical Systems, and Bifurcations of Vector Fields* (New York: Springer) 484 pp
[2] Aref H 2002 The development of chaotic advection *Phys. Fluids* **14** 1315–25
[3] Ottino J M 1989 *The Kinematics of Mixing: Stretching, Chaos, and Transport* (Cambridge: Cambridge University Press) 364 pp
[4] Samelson R M and Wiggins S 2006 *Lagrangian Transport in Geophysical Jets and Waves* (New York: Springer) 147 pp
[5] Koshel K V and Prants S V 2006 Chaotic advection in the ocean *Phys.–Usp.* **49** 1151–78
   Koshel K V and Prants S V 2006 Chaotic advection in the ocean *Usp. Fizicheskikh Nauk* **176** 1177–206
[6] Samelson R M 1992 Fluid exchange across a meandering jet *J. Phys. Oceanogr.* **22** 431–40
[7] Duan J Q and Wiggins S 1996 Fluid exchange across a meandering jet with quasi-periodic time variability *J. Phys. Oceanogr.* **26** 1176–88
[8] Prants S V, Budyansky M V, Uleysky M Yu and Zaslavsky G M 2006 Chaotic mixing and transport in a meandering jet flow *Chaos* **16** 033117
[9] Uleysky M Yu, Budyansky M V and Prants S V 2007 Effect of dynamical traps on chaotic transport in a meandering jet flow *Chaos* **17** 024703
[10] Haynes P H, Poet D A and Shuckburgh E F 2007 Transport and mixing in kinematic and dynamically consistent flows *J. Atmos. Sci.* **64** 3340–51
[11] Pierrehumbert R T 1991 Chaotic mixing of tracer and vorticity by modulated traveling Rossby waves *Geophys. Astrophys. Fluid Dyn.* **58** 285–319
[12] Yang H 1996 The subtropical/subpolar gyre exchange in the presence of annually migrating wind and a meandering jet *J. Phys. Oceanogr.* **26** 115–30
[13] Del-Castillo-Negrete D and Morrison P J 1993 Chaotic transport by Rossby waves in shear flow *Phys. Fluids* A **5** 948–65
[14] Ngan K and Shepherd T 1997 Chaotic mixing and transport in Rossby-wave critical layers *J. Fluid Mech.* **334** 315–51
[15] Cencini M, Lacorata G, Vulpiani A and Zambianchi E 1999 Mixing in a meandering jet: a Markovian approximation *J. Phys. Oceanogr.* **29** 2578–94

[16] Yuan G C, Pratt L J and Jones C K R T 2002 Barrier destruction and Largangian predictability at depth in a meandering jet *Dyn. Atmos. Oceans* **35** 41–61

[17] Weiss J B and Knobloch E 1989 Mass transport by modulated travelling waves *Phys. Rev.* A **40** 2579–89

[18] Bower A S 1991 A simple kinematic mechanism for mixing fluid parcels across a meandering jet *J. Phys. Oceanogr.* **21** 173–80

[19] Zaslavsky G M 2002 Dynamical traps *Physica* D **168–169** 292–304

[20] Press W H, Teukolsky S A, Vetterling W T and Flannery B P 1992 *Numerical Recipes in C* (Cambridge: Cambridge University Press) 994 pp

[21] Zaslavsky G M 2005 *Hamiltonian Chaos and Fractional Dynamics* (Oxford: Oxford University Press) 421 pp

[22] Sommeria J, Meyers S D and Swinney H L 1989 Laboratory model of a planetary eastward jet *Nature* **337** 58–62

[23] Solomon T H, Holloway W J and Swinney H L 1993 Shear flow instabilities and Rossby waves in barotropic flow in a rotating annulus *Phys. Fluids* A **5** 1971–82